

Deep-learning climate emulator ACE2 reveals a global decrease in tropical cyclone frequency in the 15th Century under an El Niño-like sea surface temperature pattern

Mu-Ting Chien¹, Wenchang Yang², Eric D. Maloney³, Gabe Vecchi², & Elizabeth A. Barnes^{1,2,3}

¹ Faculty of Computing and Data Sciences, Boston University, USA

² Department of Geosciences, Princeton University, USA

³ Department of Atmospheric Science, Colorado State University, USA

⁴ Department of Earth and Environment, Boston University, USA

Contact: Mu-Ting Chien (mchien@bu.edu)



Submitted to Science Advances in Mar 3, 2026

This is a non-peer-reviewed preprint submitted to EarthArXiv.

FRONT MATTER

Title

Deep-learning climate emulator ACE2 reveals a global decrease in tropical cyclone frequency in the 15th Century under an El Niño-like sea surface temperature pattern

Authors

Mu-Ting Chien,^{1*} Wenchang Yang², Eric D. Maloney³, Gabriel A Vecchi², & Elizabeth A. Barnes^{1,3,4}

Affiliations

¹ Faculty of Computing and Data Sciences, Boston University, USA.

² Department of Geosciences, Princeton University, USA.

³ Department of Atmospheric Science, Colorado State University, USA.

⁴ Department of Earth and Environment, Boston University, USA.

Abstract

The relatively short modern observational record limits our understanding of the relationship between global tropical cyclone (TC) frequency and sea surface temperature (SST), resulting in uncertain future TC projections. Using novel deep-learning-based past-millennium simulations with the Ai2 Climate Emulator version 2 (ACE2), we provide insight into the connections between SSTs and TCs. ACE2 simulations reveal that the Atlantic and global tropical cyclone numbers decreased in the 15th Century under an El Niño-like SST pattern, consistent with the high-resolution dynamical climate model HiRAM, and Atlantic sediment proxies. Global TC frequency decreased mainly due to stronger vertical wind shear and the drier midtroposphere as the Hadley circulation strengthened. Conversely, global TC frequency would increase under a La Niña-like SST pattern, as shown in idealized SST experiments with ACE2. This study demonstrates an exciting opportunity to examine TC-climate interactions using deep-learning-based paleoclimate simulations and highlights the need to constrain future projections of SST patterns to accurately estimate TC frequency.

Teaser

Global and North Atlantic tropical cyclones decline under equatorial warming, revealed by past-millennium deep-learning simulations and sediments.

MAIN TEXT

Introduction

Since all impacts of tropical cyclones (TCs) require the existence of a TC, accurate predictions of annual tropical cyclone (TC) frequency lead to better societal planning for damage mitigation. However, predicting TC frequency remains challenging because our understanding of its relationship with large-scale climate is limited, owing to the

47 complexity of multi-scale interactions and the short modern instrumental record (1). To
48 date, no significant trend in global TC frequency has been observed in the short
49 instrumental record (~80 years), even with the emergence of a climate change signal in
50 surface temperatures (1, 2). Future projections of tropical cyclone numbers under climate
51 change also remain uncertain (3), with many global climate models suggesting a global
52 decrease in TC frequency, and other models and statistical downscaling studies predicting
53 a global increase in TC frequency under warming scenarios of the 21st Century (1-6).
54 These conflicting results indicate a lack of consensus on how large-scale climate (i.e., sea
55 surface temperature (SST) patterns) would change under greenhouse gas-induced warming
56 (7) and how they control the global tropical cyclone frequency (7-11).

57 Examining tropical cyclone frequency over the past millennium, long before the modern
58 instrumental era, is a promising way to disentangle the relationship between long-term
59 climate states (or SST patterns) and TC frequency (12-15). When examining the past,
60 scientists use proxy data from corals, tree rings, and ocean sediments to infer past SSTs
61 (16) and even approximate the number of tropical cyclones in some regions (14, 15).
62 However, these paleo proxy data are sparse in space and time, and thus, global simulations
63 are often necessary to obtain output that is spatially consistent and temporally continuous.
64 Numerical simulations of TCs are traditionally performed by high-resolution global
65 climate models that have a good representation of TC numbers (3), but are extremely
66 expensive to run. The latest evidence from sediment-based TC proxies suggests that one
67 of the largest decreases in Atlantic TC numbers over the past millennium occurred
68 between 1351 AD and 1550 AD, as the climate transitioned to the Little Ice Age (15).
69 However, (15) did not run high-resolution global climate models that explicitly resolve
70 TCs, making it difficult to comprehensively discuss what environmental factors may have
71 led to this possible TC change.

72 In recent years, deep-learning climate emulators (AI emulators) have emerged and offer
73 more simulations at lower computational costs, potentially serving as an alternative tool
74 for long-term climate simulations (17-21). These AI emulators are trained on reanalysis or
75 dynamical global climate models and demonstrate good representation of climate
76 variability (17-20), and even extreme weather events (22, 23, 24). AI emulators have been
77 shown to exhibit a realistic representation of past heatwaves and cold events up to the
78 beginning of the 20th century, decades outside of their training period (25). While tropical
79 cyclone (TC) variability and its relationship with environmental conditions in the current
80 climate are found to be well simulated in a deep-learning emulator, the Ai2 Climate
81 Emulator Version 2 (ACE2) (22, 23), the extent to which AI emulators can be used to
82 simulate climates outside of their historical training period (e.g., the past millennium) is
83 currently at the forefront of their uptake. If the AI emulators can simulate the past
84 millennium TCs well, they will provide a unique opportunity to examine TC-climate
85 interactions through various experiments at high computational efficiency — a novelty of
86 this study.

87 Driving questions for this research are as follows: First, how well can a deep-learning
88 climate emulator, ACE2, simulate global TC frequency changes during the transition to
89 the Little Ice Age, specifically from 1351 to 1550 AD? Second, what role did SSTs play in
90 modifying global TC frequency from 1351 to 1550 AD? Examining preindustrial climate
91 allows us to focus on the natural variability of TC frequency and SSTs. By combining the
92 efficiency of a deep-learning climate emulator with paleoclimate records, we aim to build
93 a fundamental understanding of SST patterns and global TC frequency.

94 We perform the first sets of TC-resolving global simulations from 1351 to 1550 AD using
95 (i) a deep-learning climate emulator ACE2 and (ii) a high-resolution dynamical model
96 HiRAM forced with the SST boundary conditions. The simulations are compared with
97 sediment proxy data of Atlantic tropical cyclones as our baseline for validation. We also
98 systematically examine the effects of SSTs on global TC frequency by running various
99 idealized SST pattern experiments in ACE2, fully leveraging the fast computation of
100 ACE2. Our paleo TC diagnostic using the seed-probability framework (26-28) has
101 implications for future changes in TC frequency.

103 Results

104 Atlantic and global TC decreases in the 15th century

105 We force ACE2 and HiRAM with SSTs and sea ice from 1351 to 1550 AD using last-
106 millennium reconstruction datasets (LMR 2.1, 16, 29) and track TCs across the
107 simulations using 6-hourly data (see Materials and Methods). Global TC frequency across
108 all ACE2 ensemble members depicts a clear decrease in the 15th century (from 1401 to
109 1500 AD), in agreement with the single HiRAM simulation (Fig. 1A). The global TC
110 frequency decreases by 13.1% from the highest activity during 1401-1420 AD (hereafter
111 termed the High period) to the lowest activity during 1461-1480 AD (hereafter termed the
112 Low period) in the ACE2 ensemble mean. The ensemble mean annual TC counts drop by
113 13.2% (from 37.8/year to 32.8/year). The simulated decrease in TC frequency occurs
114 across all ACE2 members in most basins except the Western Pacific (green shading in Fig.
115 1B). Focusing on the Atlantic Ocean, the Atlantic 40-year lowpass TC number also
116 decreases in all members of ACE2 and a single member of HiRAM in the 15th Century
117 (Fig. 2A).
118

119 The simulated Atlantic TC frequency change in the 15th century is validated by the
120 sediment-overwashed proxy of Atlantic TC number (see Materials and Methods), also
121 showing more TCs in the early 15th century and fewer TCs in the late 15th century (Fig.
122 2B). Although the exact timing of the peaks and troughs of TC activity slightly differ
123 across ACE2 members and sediment proxy (due to internal atmospheric variability), the
124 overall decrease in Atlantic TC activity in the 15th century is consistent across all data
125 sources (Fig. 2, Fig. S1). The sediment-based proxy data are currently the best estimate of
126 Atlantic TC activity over the past millennium (15). This estimation generally agrees with
127 modern observations of TCs, although some discrepancies remain in the mid-19th century
128 and late 20th Century likely due to the limited number of sites. The sediment-based
129 estimation of Atlantic TC activity over the past millennium depicts one of the largest
130 drops in the 15th century (i.e., roughly the beginning of the Little Ice Age) (15), motivating
131 our study to focus on this period.

132 Despite the constraints of each dataset: the dynamical HiRAM model (e.g., the use of
133 cumulus parameterization), the AI emulator (e.g., trained on the current climate
134 reanalysis), and the sediment-based TC estimate (e.g., limited site numbers), three lines of
135 evidence show the same signal that Atlantic TC frequency decreased in the 15th century.
136 The reconstructed temperature and sea ice data used to force the ACE2 and HiRAM
137 simulations are based on estimates from coral reefs, tree rings, and sediment and ice core
138 measurements, and are thus independent of the sediment-overwashed estimate of TC
139 numbers. Validation of the Atlantic TC change across ACE2, HiRAM, and the sediment

140 proxy indicates that both simulations are likely comparable to observations, supporting the
141 realism of the global TC decrease in the 15th century (Fig. 1A). These results further
142 support that the AI climate emulator may learned the relationship between TC frequency
143 and SST patterns from the training data in the current climate.

144 But why did TC activity decrease in most basins from the High to the Low period in the
145 15th century (Fig. 1B)? The consistent decrease in global TC frequency in ACE2 and
146 HiRAM is most likely due to their shared SST forcing. The global mean SST decreased by
147 0.5 K from the High (1401-1420 AD) to the Low (1461-1480 AD) period (Fig. 1C), with
148 all tropical oceans but the warm tongue exhibiting cooling from the High to the Low
149 period (Fig. 1D). Two major volcanic eruptions, which produced over 10 Tg stratospheric
150 sulphate injection, occurred in 1452-1453 AD and 1459-1460 AD (green lines in Fig. 1C)
151 (30). The volcanic eruptions likely contributed to the cooling of the global mean
152 temperature during the Low period, as they released sulfate aerosols into the stratosphere,
153 which blocked incoming solar radiation to the surface (30). One possible hypothesis for
154 the global decrease in TC frequency is attributed to the global mean SST cooling. The
155 theoretical basis for this argument is that TCs occur only when SSTs are sufficiently warm
156 to provide an abundant sensible and latent heat source (31), which aligns with some
157 dynamical models and the statistical downscaling approach that predicts an increase in TC
158 activity with warming (3-5).

159 On the other hand, SST patterns (rather than the global mean SST) have also been shown
160 to affect regional TC frequency (7-11). Expanding on this idea, here, we focus on the
161 changes in SST patterns between the High and Low periods. SST decreased in most
162 tropical oceans, except that warming occurs in the equatorial cold tongue region in the
163 Pacific, resembling an El Niño-like anomaly pattern (Fig. 1D).

164 The deviation of global mean SST over the entire period (1401-1500 AD) from the current
165 climate (1950-1980) is less than 0.2 K; this small deviation is within the interannual
166 variability of SST during the training period of ACE2, further supporting the possible use
167 of ACE2 to investigate this paleo period.

168 A natural question arises: Was the decrease in global TC frequency resulted from global
169 mean SST cooling or from the specific SST pattern? This motivates us to perform
170 idealized experiments with different SST patterns by leveraging the computational speed
171 of ACE2.

172 **Global TC decreases under an El Niño-like SST trend**

173 We perform several idealized time-slice experiments with different SST patterns in ACE2
174 to decompose the effects of the anomalous SST mean and pattern on global TC frequency
175 changes (see Materials and Methods for details). The control run (CTL) represents the
176 High period, prescribed with the climatological mean SST between 1401 and 1420 AD.
177 The SST of CTL shows a similar Indo-Pacific and Atlantic warm pool as in the current
178 climate (Fig. S2B). Experiment 1 (EXP1) represents the Low period, as prescribed by the
179 mean SST between 1461 and 1480 AD. The SST anomaly in EXP1 relative to the CTL
180 resembles an El Niño-like pattern (Fig. 1D and Fig. 3A), except that stronger cooling
181 occurs on the west coast of Mexico over the Eastern Pacific. We also run three additional
182 experiments with SST anomalies modified from EXP1 to test the importance of equatorial
183 cold-tongue warming/cooling, while keeping the global mean SST the same as in EXP1.
184 Thus, comparing the response of global TC frequency to different SST patterns directly

185 tells us the effect of SST patterns under the same global mean cooling. We run the CTL
186 for 80 years (i.e., 80 ensemble members) and the remaining four experiments (EXP1-
187 EXP4) for 40 years, with each year representing a different ensemble member (i.e., 40
188 ensemble members). The initialization is described in the Materials and Methods.
189 Performing these experiments is only possible thanks to the high computational speed of
190 AI emulators.

191 Under El Niño-like SST change (EXP1), almost 75% of the 40 members predict a
192 decrease in TC number compared to CTL, yielding a p-value of 0.0032 from binomial
193 testing (Fig. 3E, see Materials and Methods for details of statistical test). In other words,
194 the global decrease in TC frequency (about 3 TCs, as shown in Fig. 3F, black bar) is
195 significant at the 99.9% confidence level. TC frequency decreases in most basins in EXP1,
196 except in the Western Pacific, where TC frequency slightly increases (Fig. 3F). Overall,
197 this leads to a 7.5% decrease in global TC frequency.

198 If warming occurs only over the equatorial cold tongue with uniform cooling elsewhere
199 (EXP2, Only-cold-tongue-warming, Fig. 3B), the global TC frequency is still more likely
200 to decrease, although the significance level is lower than in EXP1 (Fig. 3E). The decrease
201 in global TC frequency in the Only-cold-tongue-warming (-3.5%) comes from the
202 decrease in TCs in several basins, including the Northeastern Pacific (NEP), the North
203 Atlantic (NATL), and the Southern Indian Ocean (SI) (Fig. 3G). The fact that TC
204 frequency is still more likely to decrease at the 87% confidence level suggests that
205 equatorial cold-tongue warming may play a significant role in the global decrease in TC
206 frequency.

207 The response of global TC frequency in the absence of cold-tongue warming is much less
208 clear (EXP3, No-cold-tongue-warming, Fig. 3C) (Fig. 3E). Although the global mean TC
209 frequency still decreases (-2.7%), the decrease is less so than in Experiment 1, due to a
210 compensating effect of increasing TCs in NWPAC and decreasing TCs in NEP and NIO
211 (Fig. 3H).

212 Moreover, global TC frequency increases under cold-tongue cooling (EXP4, La Niña-like,
213 Fig. 3D) at a significance level of 99.5% or higher (Fig. 3E). Global TC increases by 2.9%
214 in this experiment due to an increased TC activity in most basins except NEPAC (Fig. 3I).

215 In summary, compared to the mean and median global TC number in CTL, the El Niño-
216 like and Only-cold-tongue-warming experiments show lower TC activity, the No-cold-
217 tongue-warming experiment shows similar TC activity, and the La Niña-like experiment
218 shows higher TC activity (Fig. S3). These experiments suggest that if the equatorial cold-
219 tongue does not exhibit a large anomaly, the resulting TC frequency change is less robust,
220 as shown by the biggest interquartile range in the No-cold-tongue-warming experiment
221 among all experiments (Fig. S3). From this we conclude that equatorial warming/cooling
222 strongly influences whether global TC frequency decreases or increases.

223 These idealized experiments establish a strong link between the global TC frequency
224 change and the cold-tongue SST variability, rather than the global mean SST change.
225 While the cold-tongue SST warming is associated with global TC decrease, cold-tongue
226 SST cooling is associated with global TC increase.

227 **Why does global TC frequency decrease under an El Niño-like SST change?**

We adopt the seed-probability framework (26-28) to examine why the global TC frequency decreases under the El Niño-like SST pattern from CTL to Experiment 1. The framework assumes tropical cyclogenesis as a two-step process: first, forming the precursor disturbance (i.e., seeds), and second, these seeds intensifying into TCs. This framework approximates the number of TCs as the number of seeds multiplied by the probability of intensifying to a TC:

$$N_{TC} = N_{Seed} * Probability. \quad [1]$$

Probability is calculated from three monthly mean environmental conditions (26, see Materials and Methods for more details), including (i) the potential intensity (PI), the theoretical likelihood of TCs to intensify based on the heat engine assumption, with the efficiency of the heat engine proportional to the temperature difference between the surface and the upper troposphere, (ii) the vertical wind shear (shear), which is the magnitude of the horizontal vector wind difference between 850 and 200 hPa, and (iii) the moist entropy deficit (moist), which is the ratio between the mid-troposphere moisture deficit and the boundary layer moisture deficit; a larger moist entropy deficit represents a drier mid-troposphere under the same boundary layer moisture. The probability of a seed intensifying into a TC is largest in the Northwestern Pacific and Southern Pacific to the west of the dateline (180°E) in CTL (Fig. S4A), mainly due to lower saturation moisture deficit (moister mid-troposphere) (Fig. S4B), larger potential intensity (Fig. S4C), and smaller vertical windshear (Fig. S4D).

We also explicitly track seeds in CTL and EXP1 (see Materials and Methods) from ACE2. The number of seeds is generally 2.6 times that of TCs because not all seeds become TCs (Fig. S5). Despite different seasonal cycles of seeds and probability (Fig. S6, solid vs. dashed lines), the seasonal cycle of seeds multiplied by probability (Fig. 4A-F, dotted line) can capture the seasonal cycle of simulated TCs (Fig. 4A-F, solid line). For example, in the North Atlantic, the change in seeds shows a more drastic onset after June, while the change in probability is more gradual (Fig. S6); however, considering seeds and probability together better captures the seasonality of observed TCs (Fig. 4C, 27). Using seeds and probability together can capture the seasonal cycle of TCs across all basins, with a linear regression coefficient of $R^2=0.92$ (Fig. 4G). Thus, TC genesis in ACE2 is likely physical (22, 23), and we can use the seed-probability framework to analyze the decrease in global TC frequency from CTL to Experiment 1 (Fig. 5G).

The global decrease in TC frequency from CTL to EXP1 is mostly driven by a decrease in transition probability (relative contribution 80.6%), while the decrease in seeds contributes only slightly (relative contribution 19.2%) (Fig. 5O). The relative contribution is quantified by fixing either probability or seeds as in CTL, and comparing with the actual TC change. Global seed number shows little change from CTL to EXP1, due to compensating effects of increased seeds in SWPAC and NWPAC and decreased seeds in other basins (Fig. 5B, 5H). Contrastingly, the probability decreases in all off-equatorial basins (polar to 10°N/S) where TCs typically form (Fig. 5C, I). Probability change is the dominant driver of the global TC decrease, regardless of the different seed-tracking criteria we used (Fig. S7).

Among all factors that affect probability, the saturation moisture deficit and wind shear together account for 68.6%, and the contribution due to potential intensity is 13.1% (Fig. 5O). The probability for each factor is quantified using monthly data for that factor in

273 EXP1, while keeping the other factors fixed as in CTL. The probability change due to
274 vertical wind shear qualitatively resembles the overall probability change, showing an
275 overall decrease in off-equatorial regions, with some increase in some equatorial regions
276 and the Eastern Pacific (Fig. 5D). Furthermore, the probability change due to saturation
277 moisture deficit shows an overall global decrease in all basins except in the equatorial
278 Pacific (Fig. 5E, K), resembling the probability change due to all factors despite a lower
279 magnitude. On the other hand, the change in probability due to potential intensity is small
280 compared to the total probability, suggesting that potential intensity is not the dominant
281 reason for the probability drop (Fig. 5F). The probability change across the ACE2
282 ensemble due to each factor is consistent with that of the single ensemble member of
283 HiRAM (Fig. S8), showing increasing shear and mid-tropospheric drying in the 15th
284 Century.

285 In summary, global TC frequency decreases under El Niño-like SST because equatorial
286 warming (Fig. 6A) favors stronger equatorial convection (Fig. 6B), which strengthens the
287 Hadley circulation and, in turn, is associated with stronger subsidence drying and larger
288 wind shear in the off-equatorial regions (Fig. 6C, 6E). Drier mid-troposphere and larger
289 wind shear hinder TC genesis. The change in the meridional overturning circulation and
290 its effect on TC genesis is consistent across SST experiments. As the meridional SST
291 gradient increases across experiments (from La Niña-like to El Niño-like experiment),
292 annual TC number decreases consecutively with the decrease in seed-to-TC probability
293 (Fig. 7A), mainly driven by the increasing vertical wind shear and larger saturation
294 moisture deficit (Fig. 7B, S9, S10). Overall, the change in the meridional SST gradient
295 largely determines whether global TC frequency increases or decreases by modifying the
296 strength of the meridional general circulation. Our results show a strong link between
297 global TC frequency and SST patterns, particularly the meridional SST gradient,
298 providing insights into future TC projections.

299 On a separate note, the regional TC change in each basin under an El Niño-like pattern is
300 more complicated than the global change, as it is a tug-of-war between regional changes in
301 probability and seed (Fig. 5G, H, I). For example, in the South Pacific (SPAC), the strong
302 probability decreases under an El Niño-like pattern outweigh the increase in seeds, leading
303 to a decrease in TC frequency. In the Northwestern Pacific (NWPAC), however, the
304 increase in seeds outweighs the decrease in probability, leading to an increase in TC
305 frequency. The El Niño-like pattern induces stronger equatorial convection in the central
306 Pacific, which also increases the seed propensity index (likelihood of seed genesis based
307 on large-scale upward motion; see 26 and Materials and Methods) right off the equator
308 over the Pacific (Fig. 6D), where planetary vorticity is nonzero. This leads to increased
309 seed counts in SPAC and NWPAC, thereby affecting regional TCs (Fig. 6F). Globally,
310 however, a small change in seed number contributes only slightly to changes in global TC
311 frequency (Fig. 5O).

312 Discussion

313 We demonstrate a framework to investigate tropical cyclone (TC) frequency in
314 paleoclimate, specifically during the transition to the Little Ice Age (1401-1500 AD),
315 using a deep-learning global climate emulator (ACE2), and compare it with dynamical
316 model simulations (HiRAM), and sediment proxy data. We show the exciting possibility
317 of using ACE2 to perform various idealized sea surface temperature pattern experiments,
318
319

320 fully leveraging its fast computation to diagnose the drivers of SST-driven global TC
321 variability. Our results suggest that SST patterns, given the same global-mean cooling,
322 largely determine whether global TC frequency increases or decreases – underscoring the
323 need to understand the mechanisms controlling patterns of SST change in efforts to
324 understand the drivers of past TC activity and predict future TC activity. Under an El
325 Niño-like SST pattern, the meridional SST gradient is larger, favoring a stronger
326 meridional overturning circulation with larger wind shear and a drier mid-troposphere,
327 producing an environment less favorable for TC genesis (Fig. 8). La Niña-like SST
328 patterns are more favorable for TC genesis as the meridional overturning circulation
329 weakens. Under the seed-probability framework, the overall change in global TC
330 frequency is dominated by changes in seed-to-TC transition probability due to wind shear
331 and mid-tropospheric humidity, whereas regional TC changes are highly dependent on
332 changes in both seeds (i.e., precursor disturbances) and probability.

333 Our results have implications for future projections of tropical cyclone frequency, as many
334 global climate models predict an El Niño-like warming pattern, whereas the observational
335 record over the current decades shows a La Niña-like warming pattern (7). We underscore
336 the need to better constrain SST projections to obtain more accurate estimates of future
337 tropical cyclone activity. Our results add to the growing literature emphasizing that the
338 pattern of SST trend has a large influence on TC frequency (7-11), with a unique
339 perspective of examining global TC frequency under the past millennium climate. A few
340 potential future research directions include expanding the time span of this analysis to the
341 entire last millennium, to find if an El Niño-like or La Niña-like trend occurs during other
342 time periods, and how global TC frequency changes in response. To further test our
343 finding (i.e., the sensitivity of global TC frequency to equatorial warming) across mean
344 climate states, future studies can conduct more idealized SST experiments based on the
345 present-day mean SST with small regional patches of warming all over the globe (e.g., the
346 Green’s function approach, 37), and systematically examine the sensitivity of global TC
347 frequency to regional warming (38). Meanwhile, the TC-SST investigation would also
348 benefit from the development of next-generation AI climate emulators with more vertical
349 levels and a more accurate representation of upper-tropospheric temperatures (see
350 Materials and Methods).

351 While future projections of TCs are highly uncertain, we demonstrate that examining TC
352 variability over the last millennium can provide insights into TC-climate interactions,
353 providing a complementary lens to exploring the modern instrumental era. The last
354 millennium provides long enough data to gain insights that we cannot obtain from recent
355 trends after the instrumental era, and the preindustrial climate provides a natural
356 laboratory for examining changes in TC frequency. For this approach to work, TC-
357 resolving simulations are necessary, and for this, we highlight the success of a deep-
358 learning emulator (ACE2). However, to comprehensively investigate past-millennium TC-
359 climate interactions, we stress the need to develop more proxy data on TC in other major
360 TC basins, such as the Western Pacific (13). More proxy data will allow us to fully
361 leverage past-millennium simulations from dynamical models and AI emulators with high
362 confidence.

363 **Materials and Methods**

364 **Ai2 Climate Emulator (ACE2)**

367 ACE2 is the second version of the Ai2 Climate Emulator (19). It is trained on the ERA5
368 reanalysis dataset (34) from 1940 to 2000, and 2010-2020. The architecture is based on
369 spherical Fourier Neural Operators (35), with an autoregressive prediction of temperature,
370 horizontal wind, humidity, surface pressure, and precipitation. The prediction is at 6-
371 hourly temporal resolution with 8 vertical levels on a sigma-pressure hybrid coordinate.
372 Forcing variables are prescribed, including SST, sea ice fraction, CO2 concentration, and
373 shortwave radiation. A unique advantage of this emulator is that it conserves global air
374 mass and moisture, which makes long-term integration possible. ACE2 is a good
375 candidate for climate modeling because it can be run stably for more than 1000 years with
376 low computational resources.

377 **High-resolution atmospheric model (HiRAM)**

378 In addition to ACE2, we also use the Princeton Geophysical Fluid Dynamics Laboratory
379 dynamical high-resolution atmospheric model (HiRAM), with 50-km horizontal
380 resolution, and 37 vertical levels (36). This model has shown good skill in representing
381 global tropical cyclone activity (37).

382 **Sediment proxy data of Atlantic TC**

383 In the Atlantic Ocean, studies have provided sediment proxy data from 12 sites along the
384 east coast of the US and the islands of the Caribbean Sea to construct the basin-wide
385 Atlantic TC activity (15). The sediment-based TC proxy data is our best estimate of the
386 basin-wide TC frequency in the North Atlantic over the past millennium. The sediment
387 data examines the number of event layers to approximate the number of tropical cyclones.
388 That is, when intense storms pass over the island, the intense rainfall and wind make
389 coarse-grained particles in the sediment more likely to occur than during normal times
390 without storms. While the sediment data are collected at different locations, a recent study
391 (15) used those data to construct basin-wide Atlantic TC activity. They combined data
392 from each site, removed duplicate TC cases, normalized by the modern observations at
393 each site, and smoothed with a 40-year low-pass filter to match the coarsest resolved
394 contributing record from an individual site. Although the sediment proxy is our best
395 estimate of Atlantic TC, it should be noted that the data are based on a limited number of
396 sites, including a complete lack of proxy data in the Southern Caribbean, Western Gulf
397 Coast, and Southeast US coast.

400 **Paleo experiment using ACE2**

401 We run 3 members of the ACE2 simulation with prescribed boundary conditions from
402 1351 to 1550 AD. The boundary conditions come from solar forcing, the last-millennium
403 reconstructed sea surface temperatures (SSTs) and sea ice, and CO2 concentrations held at
404 the preindustrial level of 280 ppm. Sea surface temperature is reconstructed from data
405 assimilation of proxy data, including temperature from coral reefs, ocean sediment, and
406 ice cores (LMR 2.1, 16). The northern hemispheric sea ice uses the reconstruction from
407 (29), while the Southern hemispheric sea ice is set to the average between 1940 and 1970,
408 since no reconstruction data are available to our knowledge. Because the reconstructed
409 SST and sea ice data are only provided annually, we obtain the 6-hourly forcing by adding
410 the average annual cycle from 1940 to 1970 in the ERA5 reanalysis at 6-hourly resolution
411 to the annual reconstructed SST and sea ice. Solar forcing is prescribed to be the same as
412 present, representing the seasonal cycle based solely on orbital parameters. Because no
413 observed atmospheric initial condition of 1351 AD exists, we obtain the initial condition
414 by running the ACE2 model for 1 year with the initial condition from the 1940 ERA5
415 reanalysis and 1350 AD boundary conditions. This initial condition is used for the first
416

417 member. To obtain the initial condition of the second member, we take the initial
418 condition of member 1 and run ACE2 with the boundary condition of 1350 AD for
419 another year, and get the final output. Similarly, we take the initial condition of member 2
420 and run ACE2 with a boundary condition of 1350 ad for one more year, and get the final
421 output as the initial condition of member 3. After getting the three initial conditions, we
422 run the ACE2 with forcings from 1351 to 1550 AD.

423 **Paleo experiment using HiRAM**

424 We take a similar approach as those above in ACE2, except that (i) we only run one
425 member of HiRAM, due to the high computational expense, (ii) we use the sea ice
426 monthly climatology over 1871-1890 from HadISST, instead of using the sea ice data
427 from reconstruction, and that (iii) SST is from LMR2.1 with bias correction following
428 (38).
429

430 **Idealized sea surface temperature experiments with ACE2**

431 In addition to the temporal evolution experiment as mentioned before, we have 5 sets of
432 time-slice experiments using different SST patterns as boundary conditions, named the
433 control run (CTL), and experiments 1-4. While the control run is run for 80 years (i.e., 80
434 ensemble members), the remaining four experiments are run for 40 years, with each year
435 representing a different ensemble member. The first member of CTL (EXP1-EXP4) is
436 initialized by the initial condition of 1401 (1461) AD. The initial condition for 1401
437 (1461) AD is obtained by running the ACE2 model for 1 year with SST boundary
438 conditions of 1400 (1460) AD. The initial conditions for the remaining members are
439 obtained from the last day of the 1-year simulation of the previous member. That is, the
440 second (third) member of the simulation is initialized by the last day of the 1-year
441 simulation of the first (second) member, and so on. The SST pattern of the control run is
442 based on the climatology of the year 1401-1420, when global TC activity maximizes
443 during the 1351-1550 AD period. The SST of the first experiment (EXP1) is obtained
444 from the climatology of the year 1461-1480 AD, when the global TC activity is
445 minimized. Figure 3A demonstrates the SST difference from CTL to EXP1, showing
446 equatorial warming over the Pacific, with cooling in other regions, and a stronger cooling
447 to the west of Mexico, which resembles an “El Niño-like pattern. Experiments 2-4 (EXP2-
448 4) are designed to elucidate each component of the SST pattern in EXP1, while keeping
449 the global mean SST the same as in EXP1. These designs allow us to examine the
450 response of global TC frequency to SST patterns, specifically the role of equatorial cold
451 tongue warming and cooling. EXP2-4 are as follows:
452

- 453 ● EXP2 is “Only-cold-tongue-warming”, in which cold-tongue warming is the same
454 as in EXP1, but uniform cooling is applied elsewhere on the globe. The SST
455 anomalies relative to CTL are shown in Fig. 3B. This experiment specifically
456 focuses on warming over the equatorial cold tongue.
- 457 ● EXP3 is “No-cold-tongue warming”, designed to further examine the effect on
458 TCs without equatorial cold-tongue warming, the opposite situation to EXP2. We
459 remove the equatorial cold tongue and add its warming uniformly to other regions
460 of the globe. The SST anomalies relative to CTL are shown in Fig. 3C. Except for
461 the cold tongue warming, the remaining tropical ocean SST anomalies are
462 qualitatively similar to those in EXP1.
- 463 ● The last experiment (EXP4) is the reversed SST anomaly pattern compared to
464 EXP1 (a “La Niña-like” pattern), where cooling occurs over the equatorial cold
465 tongue, and warming occurs elsewhere (Fig. 3D). Note that there is also a slight

466 enhanced warming off of the Mexican coast, opposite to the enhanced cooling in
467 EXP1. The SST anomalies are obtained with the reverse sign of those in EXP1
468 and, additionally, scale the magnitudes of the positive and negative anomalies to
469 keep the global mean cooling the same as in EXP1 (Fig. 3D). This is why the
470 magnitude of the anomalies is smaller in EXP4 than in EXP1. This experiment
471 provides the opposite situation to EXP1 to further investigate the effect of
472 equatorial cooling.

473 **Tropical cyclone tracking**

474 The TC tracking criteria in ACE2 identify closed contours of sea level pressure, and the
475 center of TCs when a sea level pressure minimum occurs, and 10-meter maximum wind is
476 above 10 m/s. The sea level pressure needs to decrease by 2 hPa within 5.5 deg. We use
477 the TempestExtremes package to track TCs (39), with detailed criteria same as (22).
478 TempestExtremes has two steps: the first step is to detect the center of TCs, and the
479 second step is to connect TC locations of the same storm together in time. In HiRAM, we
480 use a slightly different tracking criterion to be consistent with their previous study. We
481 track TCs in HiRAM following the algorithm developed by (36), with lifetime and
482 threshold criteria similar to (37). Because HiRAM tends to produce more TCs than
483 observed, we only detect hurricane-level TCs in HiRAM to represent its TC activities. The
484 criteria we use for TC detection in HiRAM are at least 72 hours of total lifetime, 48
485 cumulative hours of warm core, and 36 continuous hours of both warm core and max wind
486 speed > 15.75 m/s. Hurricane-level TCs are identified if the peak intensity is over 30 m/s.
487

488 Even if we use slightly different tracking criteria in ACE2 and HiRAM, it is appropriate
489 because we only compare the percent change of TCs in ACE2 and HiRAM relative to the
490 model's own baseline (i.e., the model's TC number climatology), instead of comparing the
491 absolute number of TCs. The different tracking criteria are tuned to suit each simulation
492 model.

493 TCs are abundant in each major active TC basin in 1401 to 1420 (Fig. S2A), where off-
494 equatorial sea surface temperature is relatively high (Fig. S2B). We separate TCs into 6
495 basins, including the Northern Indian Ocean (NIO, 45-105°E, 0-30°N), Southern Indian
496 Ocean (SIO, 35-135°E, 0-30°S), Northwestern Pacific (NWPAC, 105-180°E, 0-30°N),
497 South Pacific (SPAC, 135-270°E, 0-30°S), Northeastern Pacific (NEP, 180-265°E, 0-
498 30°N), and North Atlantic (NATL, 265-359°E, 0-30°N). The domain of each basin is
499 shown in Fig. 1B, following (22).

500 **Seed tracking**

501 We also track the precursor disturbance (i.e., seeds) prior to tropical cyclogenesis in ACE2
502 using TempestExtremes (39). Because there is no universal definition of seeds, we
503 combine the approaches from (27, 40), based on the variables available in ACE2. The
504 tracking criteria are based on a vorticity maximum at 850 hPa, a 99th percentile
505 precipitation threshold, and a decrease of 1 hPa in sea level pressure within 5.5 deg. Note
506 that the sea level pressure criterion is half of the TC definition, aiming to find the
507 disturbances before TC genesis. We have also tried different criteria for seeds by adjusting
508 the sea level pressure criteria to 0.5 hPa and 0.2 hPa. The key results of this paper remain
509 qualitatively similar regardless of this threshold, as shown in Fig. S7, in that the global
510 decrease in TC frequency is mostly dominated by the decrease in transition probability.
511

Analysis of the TC decadal trend

Because the year-to-year variation of TC numbers is large, we process the data to better depict the decadal trend of TCs using a 40-year low-pass Butterworth filter. The 40-year Butterworth filter is also applied to the time series between 1351 and 1550 AD, where the beginning and ending 20 years are discarded due to the biased response function (41).

Statistical analysis

After tracking TCs in idealized SST experiments in ACE2, we perform the binomial test to quantify how significant each TC season is above or below the average TC number in the control run. Figure 3E shows, across the 40 years of each experiment, how many TC seasons are more active (magenta) or less active (green) than the CTL. If SST patterns do not affect the global TC count, there will be equal numbers of active and inactive seasons (20 years each). The p-value is obtained by how significant the result of each experiment is compared to a random distribution, shown in Fig. 3E.

The seed-probability framework

Lastly, we apply the seed-probability framework to examine what environmental condition leads to the TC frequency change. The overall probability difference between the control run and Experiment 1 in HiRAM is consistent with ACE2 (Fig. S8). This seed-probability framework was first introduced in (26) based on aquaplanet simulations of the current climate with various warming and cooling experiments. We choose this framework to analyze the TC frequency change in paleoclimate because this framework has been applied successfully to explain TC frequency on various timescales and climates, including the seasonal cycle of TCs in the current climate (27), changes of TC frequency under global warming, and ENSO-like perturbations (28). We have also tried an alternative framework, which is the tropical cyclone genesis index (42), the same as the one used in our earlier study of ACE2 in the current climate (22), and found that the change in environmental conditions from 1401-1420 to 1461-1480 shows consistent results (not shown). Under the seed-probability framework, the number of TCs is approximated as the number of seeds multiplied by probability (Eq. 1), where the probability is calculated by

$$\text{Probability} = \frac{1}{1 + \left(\frac{VI}{0.014}\right)^{1.1}}, \quad [2]$$

and the ventilation index (VI, 43) is quantified by the following equation:

$$VI = \frac{\text{Shear} * X}{PI}, \quad [3]$$

where PI represents the potential intensity, shear represents vertical wind shear, and X represents moist entropy deficit. The saturation moisture deficit used to calculate probability in Eq. [1-3] is:

$$X = \frac{S_m^* - S_m}{S_0^* - S_b}, \quad [4]$$

where S_m^* is the saturation moist entropy at 600 hPa, and S_m is the environmental entropy at 600 hPa, S_0^* is the saturation moist entropy at the sea surface, and S_b is the entropy of the boundary layer. Moist entropy can be calculated using the following equation:

$$S = C_p \log \log T - R_d \log \log p_a + \frac{L_v r_v}{T} - R_v \log \log H, \quad [5]$$

where C_p is the heat capacity of dry air, p_d is the partial pressure of dry air, H is the relative humidity, R_d is the gas constant for dry air, R_v is the gas constant for water vapor, and L_v is the latent heat for vaporization. The potential intensity can be calculated by

$$PI^2 = \frac{T_s - T_o}{T_o} * \frac{C_k}{C_d} (k^* - k), \quad [6]$$

where T_s represents surface temperature, and T_o represents outflow temperature. The terms k^* and k represent the sea surface saturation enthalpy and the boundary layer enthalpy. Because ACE2 provides coarse vertical resolution (8 vertical levels), to accommodate this limitation when calculating potential intensity, we prescribe the outflow pressure level from the 37 vertical-level dynamical simulation HiRAM, rather than calculating it from ACE2. We obtain the outflow temperature in ACE2 based on the environmental temperature at 100 hPa for the deep convection region (SST > 70%), 400 hPa for the weak subsidence region, and 600 hPa for the strong subsidence region (SST < 10%). The choice of vertical levels for each horizontal grid is obtained by calculating the time average outflow levels from the vertically-fined HiRAM simulation with the same time period (1351-1550 AD). This approach is under the assumption that outflow levels are mostly determined by the SST, which is identical in HiRAM and ACE2.

Seed propensity index

Under the seed-probability framework, we use two approaches to quantify seeds, one of which is to explicitly track seeds, and the other is to approximate the seed density based on environmental conditions. The latter one is called the seed propensity index (SPI), developed by (26). Since vertical velocity is not the direct output of ACE2, we adopt the index by replacing vertical velocity at 500 hPa with precipitation, given that the monthly means of the two fields are often tightly correlated. Our calculation of the seed propensity index is as follows:

$$SPI = \text{precip} * \frac{1}{1 + Z^{-1/\alpha}}, \quad [7]$$

where precip represents precipitation rate, and Z represents normalized vorticity, which can be calculated as follows:

$$Z = \frac{f + \xi}{\sqrt{\frac{d|f + \xi|}{dy} * U}}, \quad [8]$$

where f is planetary vorticity ($2 * \Omega \sin(\phi)$), ξ is relative vorticity ($\frac{\partial v}{\partial x} - \frac{\partial u}{\partial y}$), and $U=20$ and $\alpha=0.69$ are parameters fitted from aquaplanet simulations. We relate the tracked seed density to the SPI in Fig. 6.

References

1. Sobel, A. H., Wing, A. A., Camargo, S. J., Patricola, C. M., Vecchi, G. A., Lee, C. Y., & Tippett, M. K. (2021). Tropical cyclone frequency. *Earth's Future*, 9(12), e2021EF002275.

- 604 2. Knutson, T., Camargo, S. J., Chan, J. C., Emanuel, K., Ho, C. H., Kossin, J., ... & Wu, L.
605 (2020). Tropical cyclones and climate change assessment. *Bulletin of the American*
606 *Meteorological Society*, 101(3), E303-E322.
- 607 3. Roberts, M. J., Camp, J., Seddon, J., Vidale, P. L., Hodges, K., Vanni re, B., ... & Wu, L.
608 (2020). Projected future changes in tropical cyclones using the CMIP6 HighResMIP
609 multimodel ensemble. *Geophysical Research Letters*, 47(14), e2020GL088662.
- 610 4. Emanuel, K. A. (2013). Downscaling CMIP5 climate models shows increased tropical
611 cyclone activity over the 21st century. *Proceedings of the National Academy of*
612 *Sciences*, 110(30), 12219-12224.
- 613 5. Yoshida, K., Sugi, M., Mizuta, R., Murakami, H., & Ishii, M. (2017). Future changes in
614 tropical cyclone activity in high-resolution large-ensemble simulations. *Geophysical Research*
615 *Letters*, 44(19), 9910-9917.
- 616 6. Yamada, Y., Kodama, C., Satoh, M., Sugi, M., Roberts, M. J., Mizuta, R., ... & Vidale, P. L.
617 (2021). Evaluation of the contribution of tropical cyclone seeds to changes in tropical cyclone
618 frequency due to global warming in high-resolution multi-model ensemble
619 simulations. *Progress in Earth and Planetary Science*, 8(1), 11.
- 620 7. Sobel, A. H., Lee, C. Y., Bowen, S. G., Camargo, S. J., Cane, M. A., Clement, A., ... &
621 Tippett, M. K. (2023). Near-term tropical cyclone risk and coupled Earth system model
622 biases. *Proceedings of the National Academy of Sciences*, 120(33), e2209631120.
- 623 8. Vecchi, G. A., & Soden, B. J. (2007). Effect of remote sea surface temperature change on
624 tropical cyclone potential intensity. *Nature*, 450(7172), 1066-1070.
- 625 9. Eusebi, R., Vecchi, G. A., Yang, W., & Fueglistaler, S. (2025). The Influence of Patterned
626 Warming and CO 2 on North Atlantic Hurricane Frequency. *Journal of Climate*, 38(19),
627 5391-5410.
- 628 10. Levin, E. L., Vecchi, G., & Yang, W. (2025). Influence of sea surface temperature patterns
629 and mean warming on past and future Atlantic hurricane activity.
- 630 11. Lin, J., Lee, C. Y., Camargo, S. J., Sobel, A. H., & Zhuo, J. Y. (2025). The response of
631 tropical cyclone hazard to natural and forced patterns of warming. *npj Climate and*
632 *Atmospheric Science*, 8(1), 109.
- 633 12. Zhang, G., Lin, K. E., Fu, D., Knutson, T., Franke, J., & Tseng, W. L. (2025). Chinese
634 Historical Documents Reveal Multi-Century Seasonal Shifts in Tropical Cyclone
635 Landfalls. *arXiv preprint arXiv:2502.00276*.
- 636 13. Lin, K. H. E., Tseng, W. L., Lin, Y. S., Lee, C. Y., Lin, Y. H., Hsu, H. H., & Wang, P. K.
637 (2025). Intensified tropical cyclone activity in East Asia during the Maunder (solar)
638 Minimum. *Proceedings of the National Academy of Sciences*, 122(52), e2419759122.
- 639 14. Schmitt, D., Gischler, E., Melles, M., Wennrich, V., Behling, H., Shumilovskikh, L., ... &
640 Birgel, D. (2025). An annually resolved 5700-year storm archive reveals drivers of Caribbean
641 cyclone frequency. *Science Advances*, 11(11), eads5624.
- 642 15. Yang, W., Wallace, E., Vecchi, G. A., Donnelly, J. P., Emile-Geay, J., Hakim, G. J., ... &
643 Winkler, T. S. (2024). Last millennium hurricane activity linked to endogenous climate
644 variability. *Nature communications*, 15(1), 816.
- 645 16. Tardif, R., Hakim, G. J., Perkins, W. A., Horlick, K. A., Erb, M. P., Emile-Geay, J., ... &
646 Noone, D. (2019). Last Millennium Reanalysis with an expanded proxy database and seasonal
647 proxy modeling. *Climate of the Past*, 15(4), 1251-1273.

- 648 17. Cresswell-Clay, N., Liu, B., Durran, D. R., Liu, Z., Espinosa, Z. I., Moreno, R. A., &
649 Karlbauer, M. (2025). A deep learning earth system model for efficient simulation of the
650 observed climate. *AGU Advances*, 6(4), e2025AV001706.
- 651 18. Kochkov, D., Yuval, J., Langmore, I., Norgaard, P., Smith, J., Mooers, G., ... & Hoyer, S.
652 (2024). Neural general circulation models for weather and climate. *Nature*, 632(8027), 1060-
653 1066.
- 654 19. Watt-Meyer, O., Henn, B., McGibbon, J., Clark, S. K., Kwa, A., Perkins, W. A., ... &
655 Bretherton, C. S. (2025). ACE2: accurately learning subseasonal to decadal atmospheric
656 variability and forced responses. *npj Climate and Atmospheric Science*, 8(1), 205.
- 657 20. Clark, S. K., Watt-Meyer, O., Kwa, A., McGibbon, J., Henn, B., Perkins, W. A., ... &
658 Bretherton, C. S. (2025). ACE2-SOM: Coupling an ML atmospheric emulator to a slab ocean
659 and learning the sensitivity of climate to changed CO₂. *Journal of Geophysical Research:
660 Machine Learning and Computation*, 2(4), e2024JH000575.
- 661 21. Brenowitz, N. D., Ge, T., Subramaniam, A., Manshausen, P., Gupta, A., Hall, D. M., ... &
662 Pritchard, M. S. (2025). Climate in a bottle: Towards a generative foundation model for the
663 kilometer-scale global atmosphere. *arXiv preprint arXiv:2505.06474*.
- 664 22. Chien, M. T., Barnes, E. A., & Maloney, E. D. (2025). Modulation of tropical cyclogenesis on
665 subseasonal-to-interannual timescales in the deep-learning climate emulator ACE2. *Machine
666 Learning: Earth*, 1(1), 015008.
- 667 23. Chien, M. T., Barnes, E. A., & Maloney, E. D. (2025). Modulation of Tropical Cyclogenesis
668 by the Convectively Coupled Kelvin Waves: Insights from Data-driven Climate Emulator
669 ACE2. *Geophysical Research Letters*, 53(2), e2025GL117387.
- 670 24. Duan, S., Zhang, J., Bonfils, C., & Pallotta, G. (2025). Testing NeuralGCM's capability to
671 simulate future heatwaves based on the 2021 Pacific Northwest heatwave event. *npj Climate
672 and Atmospheric Science*, 8(1), 251.
- 673 25. Meng, Z., Hakim, G. J., Yang, W., & Vecchi, G. A. (2025). Deep learning atmospheric
674 models reliably simulate out-of-sample land heat and cold wave frequencies. *arXiv preprint
675 arXiv:2507.03176*.
- 676 26. Hsieh, T. L., Vecchi, G. A., Yang, W., Held, I. M., & Garner, S. T. (2020). Large-scale
677 control on the frequency of tropical cyclones and seeds: A consistent relationship across a
678 hierarchy of global atmospheric models. *Climate Dynamics*, 55(11), 3177-3196.
- 679 27. Yang, W., Hsieh, T. L., & Vecchi, G. A. (2021). Hurricane annual cycle controlled by both
680 seeds and genesis probability. *Proceedings of the National Academy of Sciences*, 118(41),
681 e2108397118.
- 682 28. Hsieh, T. L., Yang, W., Vecchi, G. A., & Zhao, M. (2022). Model spread in the tropical
683 cyclone frequency and seed propensity index across global warming and ENSO-like
684 perturbations. *Geophysical Research Letters*, 49(7), e2021GL097157.
- 685 29. Brennan, M. K., & Hakim, G. J. (2022). Reconstructing Arctic sea ice over the Common Era
686 using data assimilation. *Journal of Climate*, 35(4), 1231-1247.
- 687 30. Toohey, M., & Sigl, M. (2017). Volcanic stratospheric sulfur injections and aerosol optical
688 depth from 500 BCE to 1900 CE. *Earth System Science Data*, 9(2), 809-831.
- 689 31. Gray, W.M., 1975. *Tropical cyclone genesis*.

- 690 32. Van Loon, S., Rugenstein, M., & Barnes, E. A. (2025). Reanalysis-based global radiative
691 response to sea surface temperature patterns: Evaluating the Ai2 climate
692 emulator. *Geophysical Research Letters*, 52(14), e2025GL115432.
- 693 33. Hsieh, T. L., Vecchi, G. A., Wang, C., Yang, W., Zhang, B., & Soden, B. J. (2024).
694 Dependence of tropical cyclone seeds and climate sensitivity on tropical cloud
695 response. *Science advances*, 10(37), eadi2779.
- 696 34. Hersbach, H., Bell, B., Berrisford, P., Hirahara, S., Horányi, A., Muñoz-Sabater, J., ... &
697 Thépaut, J. N. (2020). The ERA5 global reanalysis. *Quarterly journal of the royal
698 meteorological society*, 146(730), 1999-2049.
- 699 35. Bonev, B., Kurth, T., Hundt, C., Pathak, J., Baust, M., Kashinath, K., & Anandkumar, A.
700 (2023, July). Spherical fourier neural operators: Learning stable dynamics on the sphere.
701 In *International conference on machine learning* (pp. 2806-2823). PMLR.
- 702 36. Harris, L. M., Lin, S. J., & Tu, C. (2016). High-resolution climate simulations using GFDL
703 HiRAM with a stretched global grid. *Journal of Climate*, 29(11), 4293-4314.
- 704 37. Zhao, M., Held, I. M., Lin, S. J., & Vecchi, G. A. (2009). Simulations of global hurricane
705 climatology, interannual variability, and response to global warming using a 50-km resolution
706 GCM. *Journal of Climate*, 22(24), 6653-6678.
- 707 38. Sullivan, R. M., Wallace, E., Dee, S., Vecchi, G. A., Yang, W., & Emanuel, K. (2025). Multi-
708 centennial spatial coherency among Atlantic tropical cyclones from simulated and
709 reconstructed storm records. *Geophysical Research Letters*, 52, e2025GL116642
- 710 39. Ullrich, P. A., & Zarzycki, C. M. (2017). TempestExtremes: A framework for scale-
711 insensitive pointwise feature tracking on unstructured grids. *Geoscientific Model
712 Development*, 10(3), 1069-1090.
- 713 40. Moon, J., Kim, D., Wing, A. A., Camargo, S. J., Emlaw, G. N., Starr, J. C., & Cha, D. H.
714 (2025). Tropical cyclone seed disturbances in ERA5. *Journal of Climate*, 38(18), 4625-4639.
- 715 41. Butterworth, S. (1930). On the theory of filter amplifiers. *Wireless Engineer*, 7(6), 536-541.
- 716 42. Tippett, M. K., Camargo, S. J., & Sobel, A. H. (2011). A Poisson regression index for tropical
717 cyclone genesis and the role of large-scale vorticity in genesis. *Journal of Climate*, 24(9),
718 2335-2357.
- 719 43. Tang, B., & Emanuel, K. (2012). A ventilation index for tropical cyclones. *Bulletin of the
720 American Meteorological Society*, 93(12), 1901-1912.

721 722 723 **Acknowledgments**

724 We acknowledge scientific discussions with Emma Levin, Prof. Greg Hakim, Dr. Jihong
725 Moon, and Prof. Daehyun Kim that benefit this work.

726 727 **Funding:**

728 Heising-Simons Foundation grant #2023-4720
729 National Oceanic and Atmospheric Association (NOAA) CVP grant NA22OAR4310609
730 National Science Foundation (NSF) grant AGS-2217785
731
732
733

734 **Author contributions:**

735 Conceptualization: MC, EAB, EDM

736 Methodology: MC, WY

737 Investigation: MC, WY

738 Visualization: MC

739 Writing—original draft: MC

740 Writing—review & editing: EAB, EDM, WY, &GAV

741 **Competing interests:** All other authors declare they have no competing interests.

742 **Data and materials availability:** All analysis code is available on GitHub at
743 https://github.com/muting-chien/Paleo_global_TC_1351_1550_public.

744 **Data and materials availability:** All analysis code is available on GitHub at
745 https://github.com/muting-chien/Paleo_global_TC_1351_1550_public.

746

747

Figures and Tables

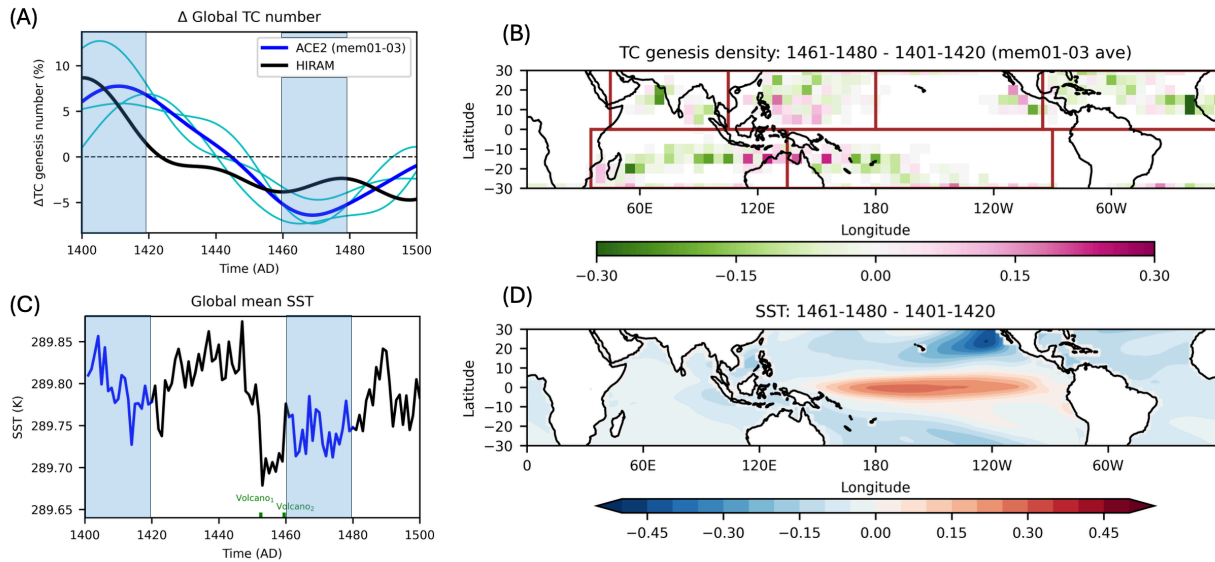
750
751
752
753
754
755
756
757
758
759
760
761
762
763
764
765
766
767
768

Figure 1. Changes in global TCs and SSTs in the 15th century. (A) Time series of the percentage change of global tropical cyclone numbers from 1401 to 1500. The light blue lines represent each ACE2-ERA5 ensemble member, with the dark blue line representing the ensemble mean. The black line represents the hurricane-level tropical cyclones in HiRAM. (B) The change in genesis density of tropical cyclones from 1401-1420 to 1461-1480 averaged across three ensemble members. The red box marks each basin. The top row from left to right represents the North Indian Ocean (NIO), the North Western Pacific (NWPAC), the North Eastern Pacific (NEPAC), and the North Atlantic (NATL), while the bottom row represents the South Indian Ocean (SIO) and the South Pacific (SPAC). (C) The global mean sea surface temperature time series from 1401 to 1500. The green horizontal lines at the bottom indicate the two volcanic eruptions in 1452-1453 and 1459-1460. (D) The change in mean sea surface temperature from 1401-1420 to 1461-1480. The light blue shadings in (A) and (C) represent the High and Low periods we focus on in this study, depicting higher and lower TC numbers in the 15th century.

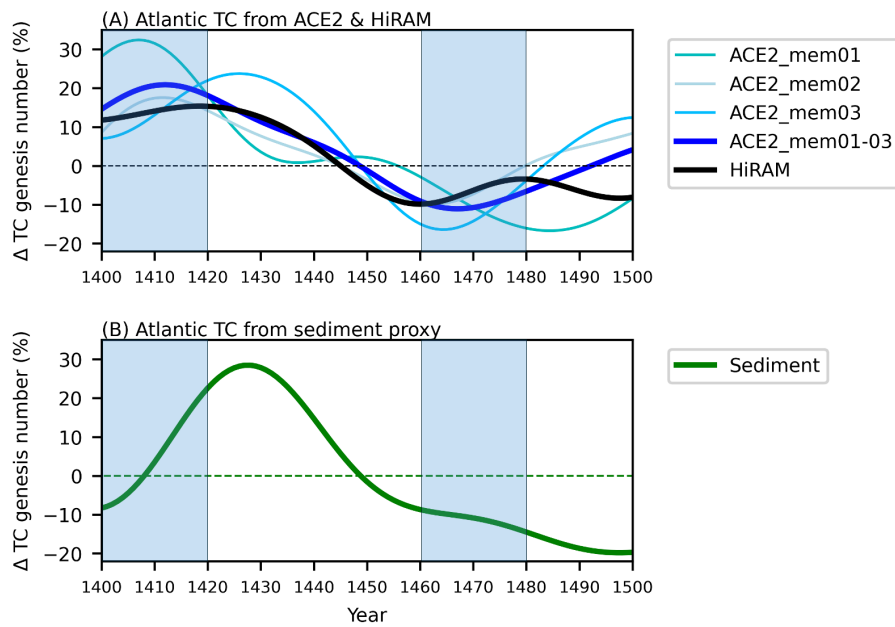


Fig. 2. Time series of Atlantic tropical cyclone (TC) number change in the 15th century. (A) The light blue lines represent each ACE2-ERA5 ensemble member, with the dark blue line representing the ensemble mean. The black line represents the hurricane-level tropical cyclones in HiRAM. The light-blue shading represents the High and Low periods. (B) The green line represents the sediment proxy TC anomalies. TC anomalies from each data are applied with a 40-year low-pass filter.

769
770
771
772
773
774
775
776
777
778

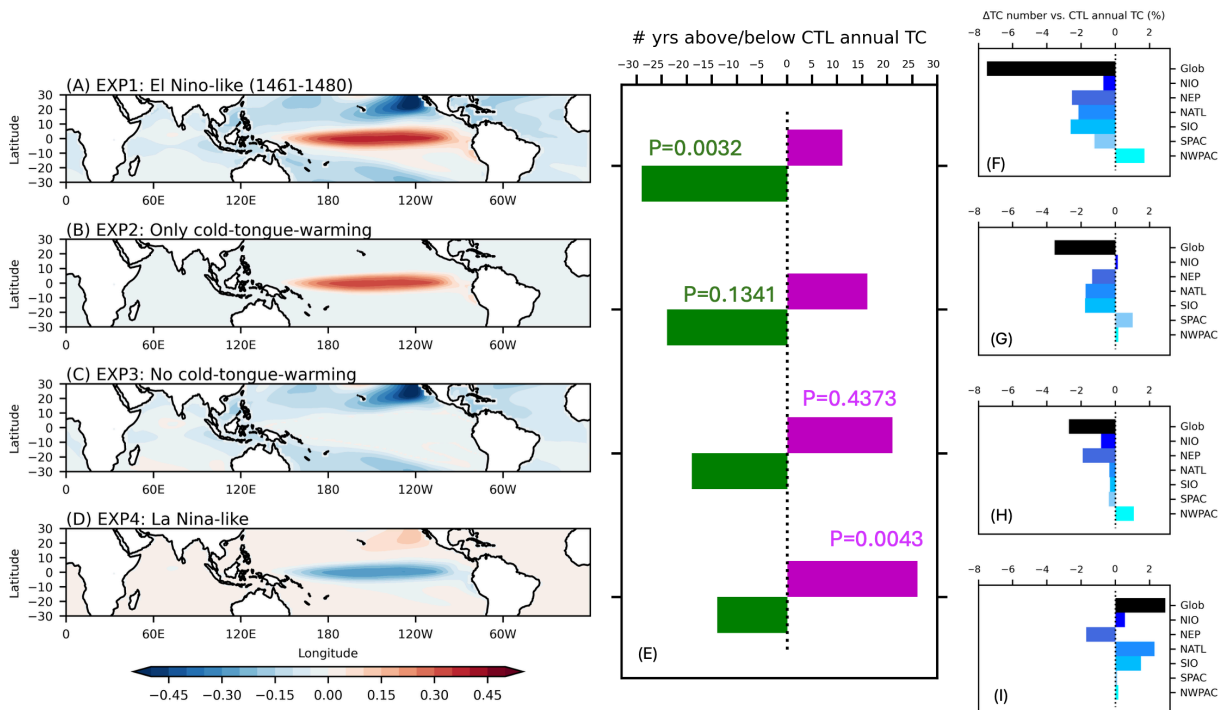


Fig. 3. Idealized sea surface temperature (SST) experiments and tropical cyclone response. (A-D) The mean SST difference compared to the control simulation (CTL) (1401-1420): (A) Experiment 1: averaged SST between 1461-1480 (El Niño-like), (B) Experiment 2: only cold-tongue-warming, (C) Experiment 3: no cold-tongue-warming, and (D) Experiment 4: La Niña-like. (E) The number of years that the tropical cyclone (TC) counts in each experiment are above (magenta bar) or below (green bar) the mean value of the TC counts in CTL. P-value for the binomial test is displayed. (F-I) The percentage change in the mean of TC number from CTL to each experiment globally (black bar) and in each basin (different blue bars). The percentage change in each basin is relative to the mean global TC number in CTL.

779
780
781
782
783
784
785
786
787
788
789
790
791
792

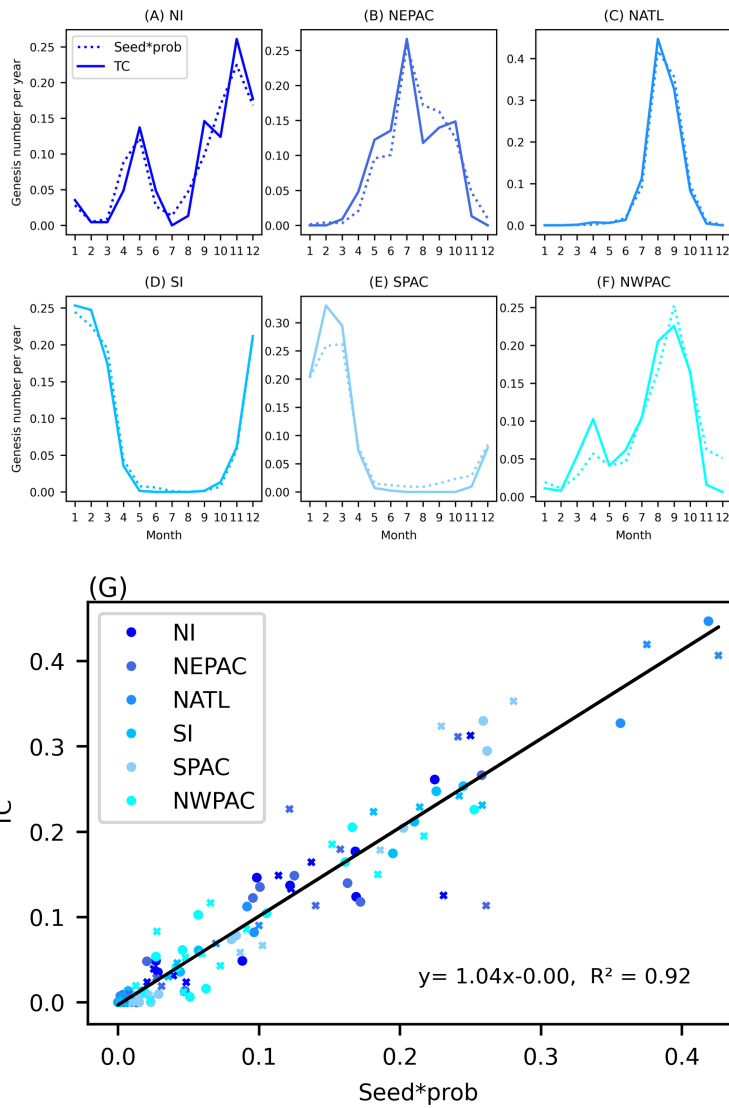


Fig. 4. Annual cycle of actual TC number and estimated TC number (i.e., seed multiplied by transition probability) after normalization. (A-F) Annual cycle of actual TC number (solid line) and estimated TC number (dotted line) in the control run in each basin: (A) North Indian Ocean (NI), (B) North Eastern Pacific (NEPAC), (C) North Atlantic (NATL), (D) Southern Indian Ocean (SIO), (E) Southern Pacific Ocean (SPAC), and (F) North Western Pacific (NWPAC). (G) Scatter plot between the annual cycle of the actual (y-axis) and estimated (x-axis) TC number for each basin. Dots represent the control run, while crosses represent Experiment 1. The linear regression line is displayed.

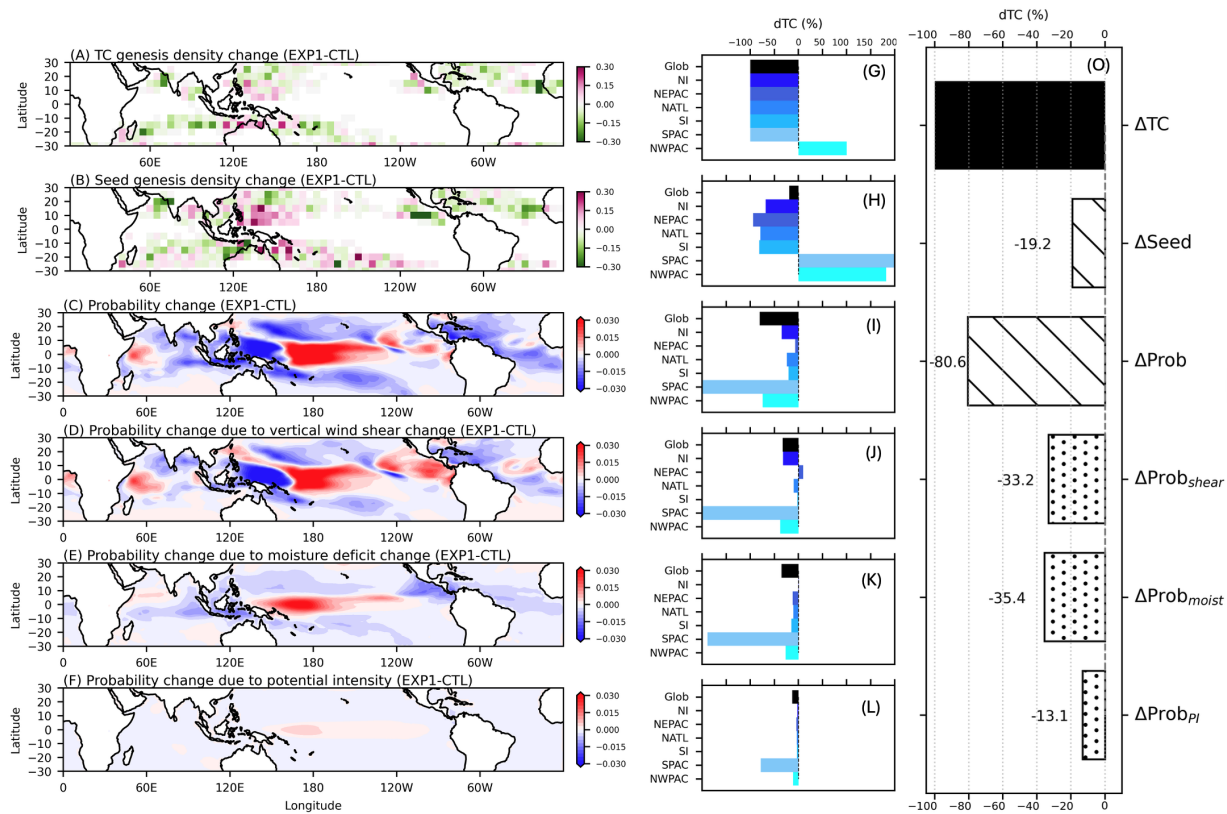
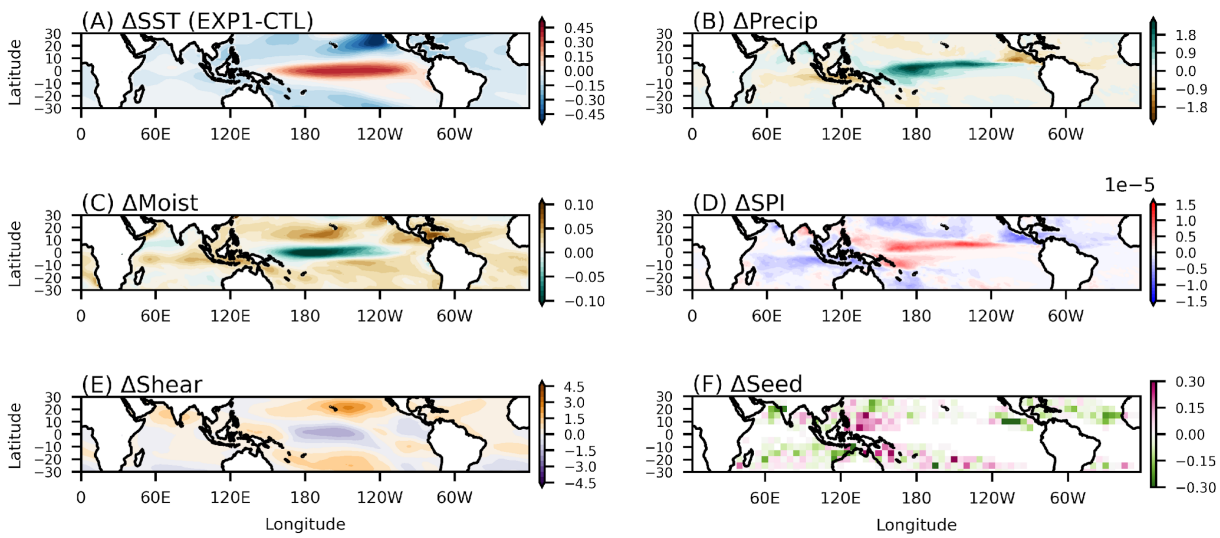


Fig. 5. Difference in seed and probability from CTL to EXP1. (A) The genesis density of tropical cyclones, (B) the genesis density of seeds, (C) the calculated transition probability from seed to tropical cyclones based on potential intensity, saturation moisture deficit, and vertical wind shear, (D-F) the calculated transition probability with a single variable in Experiment 1, while the other environmental factors are kept the same as in CTL. The single varying factor is: (D) potential intensity, (E) saturation moisture deficit, (F) vertical wind shear. (G-L) The percentage change of TC genesis number from CTL to Experiment 1 in each basin due to each factor: (G) actual TC number change, (H) seed density change, (I) probability change, (J) potential intensity change that changes probability, (K) saturation moisture deficit change that changes probability, (L) vertical wind shear change that changes probability. (O) The percentage change of the global TC number (solid bar) due to changes in seeds and probability (slanted hatch). The change in probability can be separated by changes in shear, moisture, and potential intensity (dotted hatch).



823
 824
 825 **Fig. 6. Difference in environmental conditions and seeds from CTL to EXP1.** (A) Sea
 826 surface temperature, (B) precipitation, (C) saturation moisture deficit, (D) seed
 827 propensity index based on vorticity and precipitation, (E) vertical windshear, and
 828 (F) seed genesis density.
 829

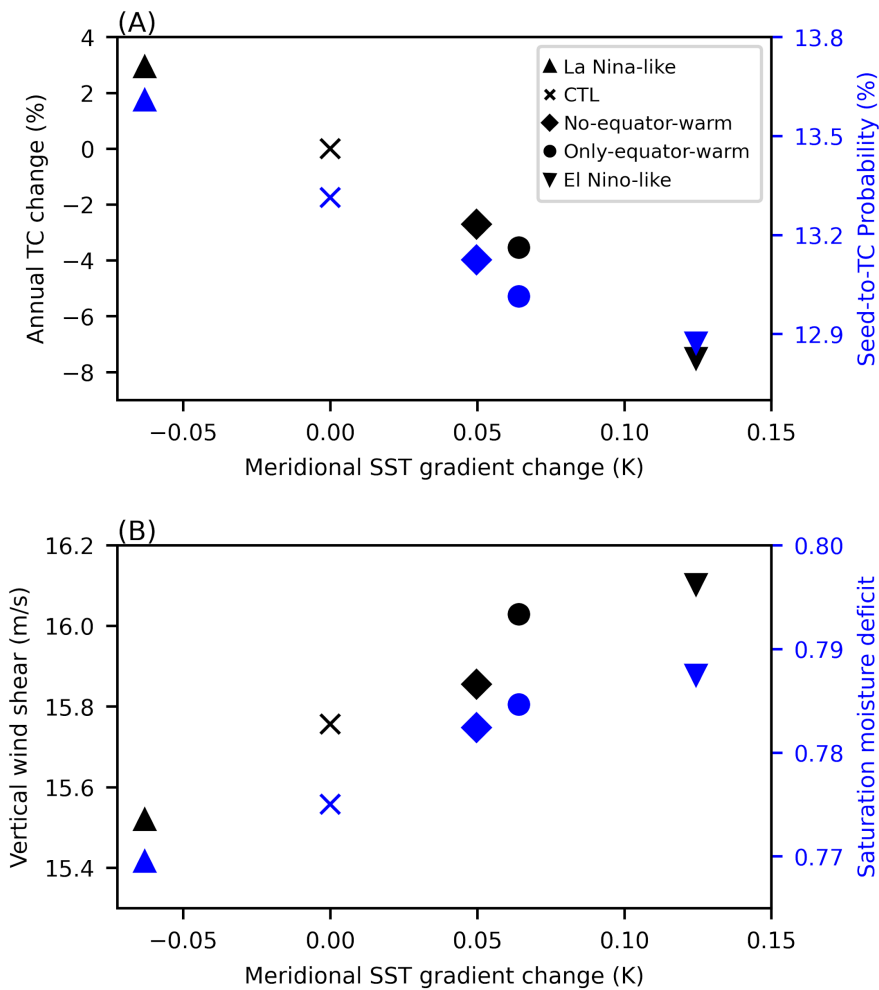


Fig. 7. Summary of the global TC and environmental conditions from each SST experiment. The X-axis represents the meridional SST gradient change from the control run, calculated from the change in SST of the equatorial region (10°S-10°N) minus the change in SST in the off-equatorial region (10-30°N/S) compared to the control run. (A) The Y-axis on the left (black) represents the annual TC number change from the control simulation, and the Y-axis on the right (blue) represents the Seed-to-TC probability. (B) The Y-axis on the left (black) represents the vertical wind shear, and the Y-axis on the right (blue) represents the saturation moisture deficit. The global mean of each quantity on the Y-axis excludes 5°S-5°N and the Southeastern Pacific and South Atlantic regions, where TC activity is rare.

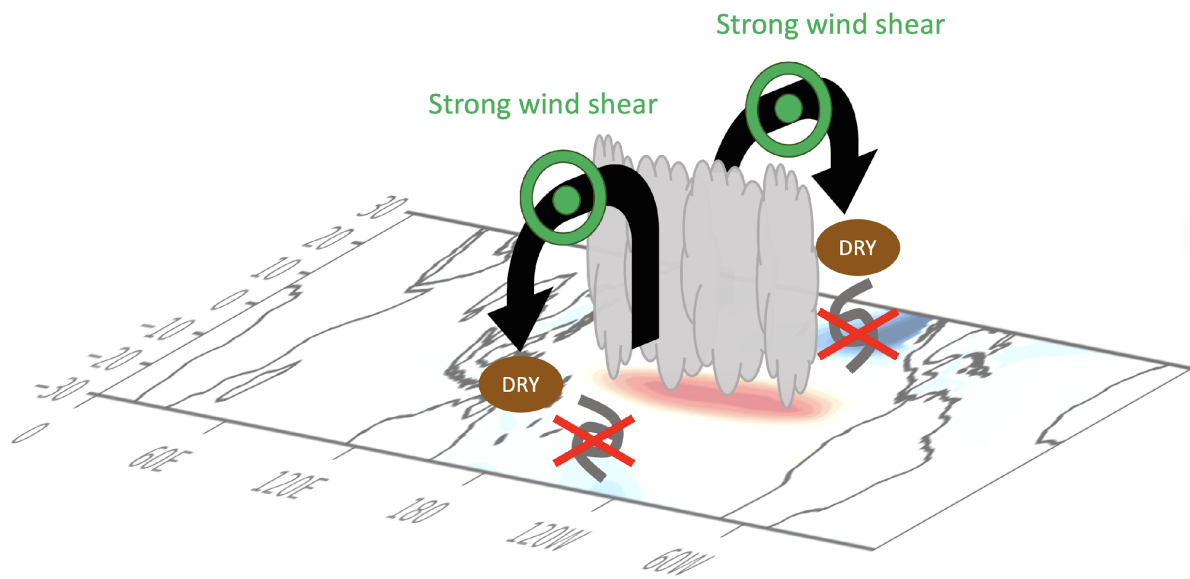


Fig. 8. Schematic of the decrease in global TC frequency under an El Niño-like SST trend. Equatorial warming induces stronger meridional circulation, stronger wind shear, and a drier midtroposphere, which are detrimental to TC genesis.

843
844
845
846
847

Science Advances



Supplementary Materials for

Deep-learning climate emulator ACE2 reveals a global decrease in tropical cyclone frequency in the 15th Century under an El Niño-like sea surface temperature trend

Mu-Ting Chien *et al.*

*Corresponding author. Email: mchien@bu.edu

This PDF file includes:

Figs. S1 to S10

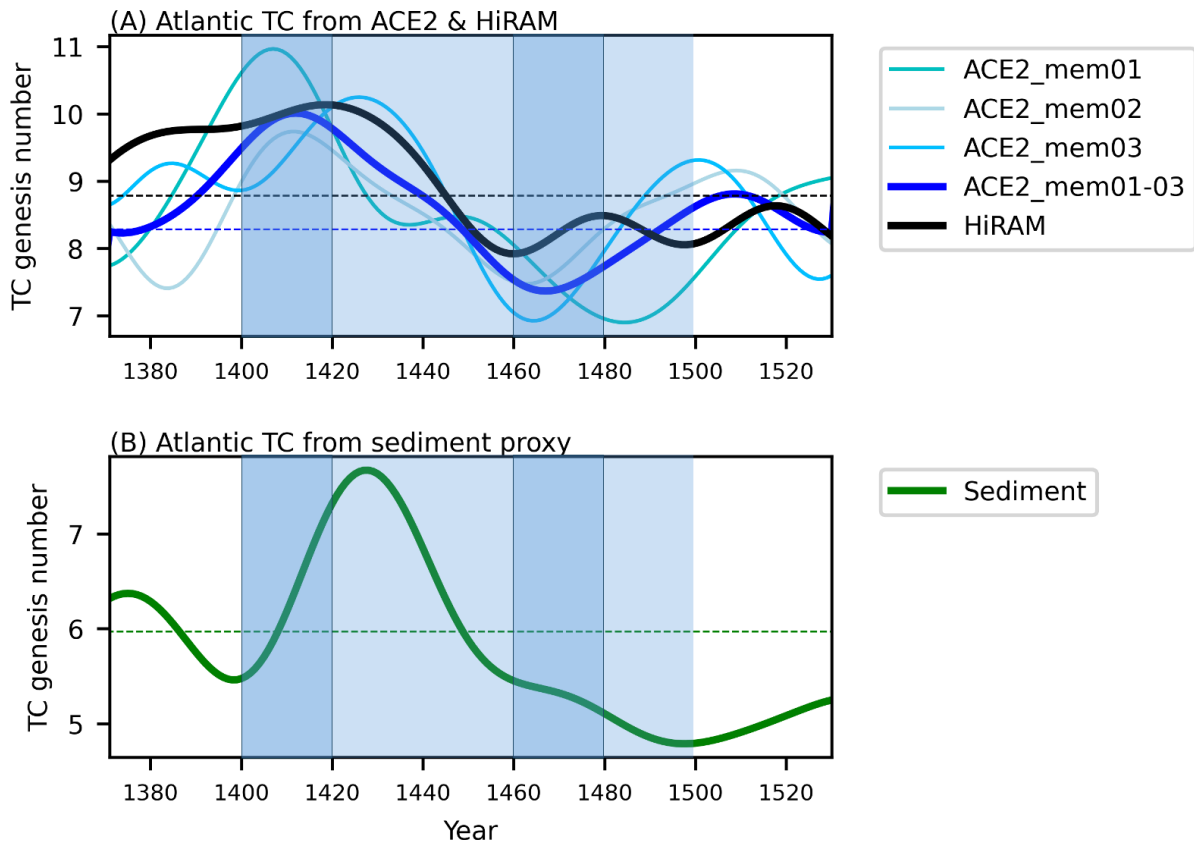


Fig. S1.

The time series of the 40-year low-pass filtered Atlantic TC number from 1371 to 1530 AD. This is similar to Fig. 2 but covers the entire simulated period. Note that the first and last 20 years (1351-1370, 1531-1550) are not shown because the 40-year low-pass filter is not applicable at the beginning and end of the simulation. The light-blue shading represents 1401-1500 AD, and the darker-blue shading represents the High and Low periods of global TCs as in Fig. 1A.

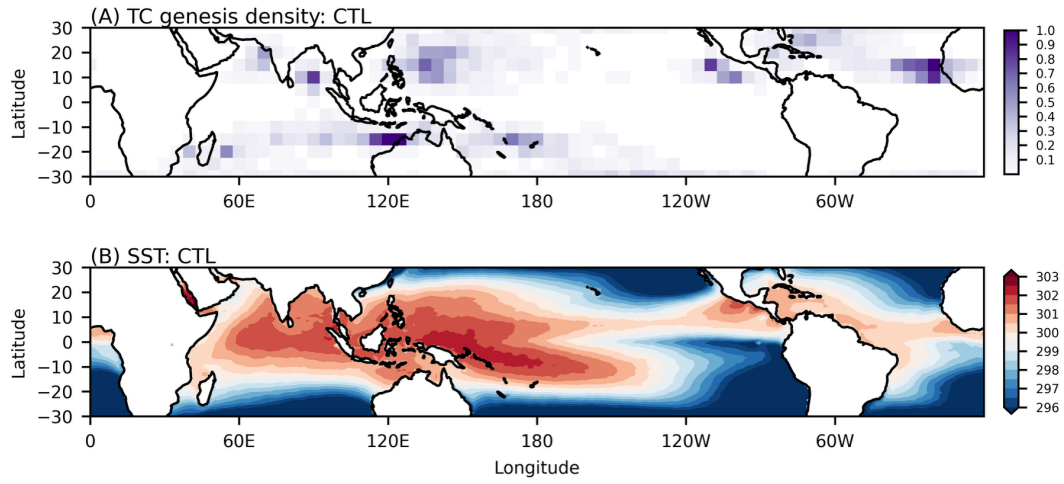


Fig. S2.

(A) TC genesis density map in 1401-1420 AD and (B) sea surface temperature map in 1401-1420 AD.

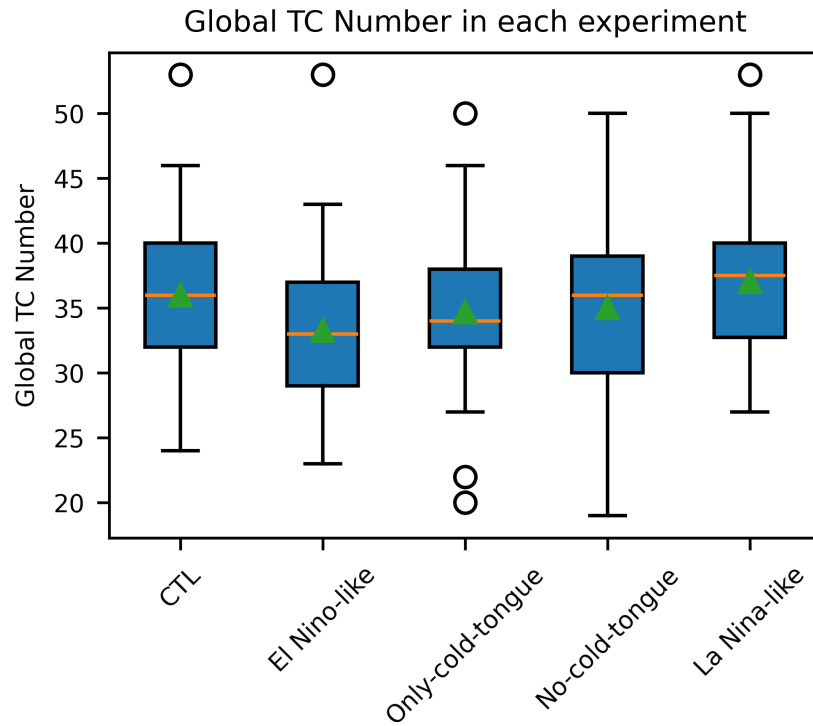


Fig. S3.

Box-and-whisker plot of TC number in each experiment for 80 ensemble members in the control run and 40 ensemble members for the other experiment. The box represents the 25th percentile and the 75th percentile, while the orange line represents the median (50th percentile). The upper and lower whiskers represent 1.5 times the interquartile range between the 25th percentile and the 75th percentile. Outliers are indicated in individual dots.

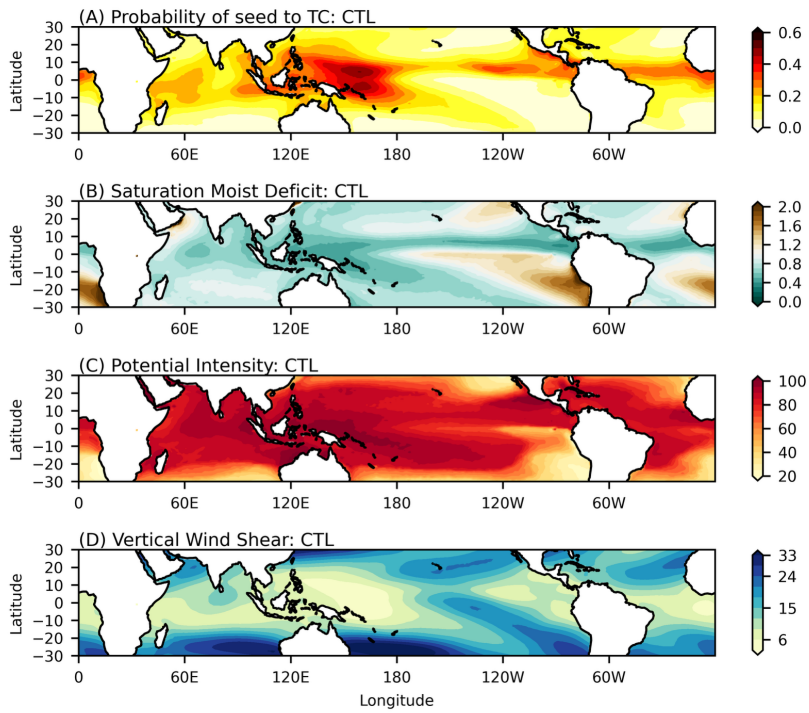


Fig. S4.

(A) Estimated transition probability from seeds to tropical cyclones based on environmental factors of the control run, including (B) saturation moisture deficit, (C) potential intensity, and (D) vertical wind shear.

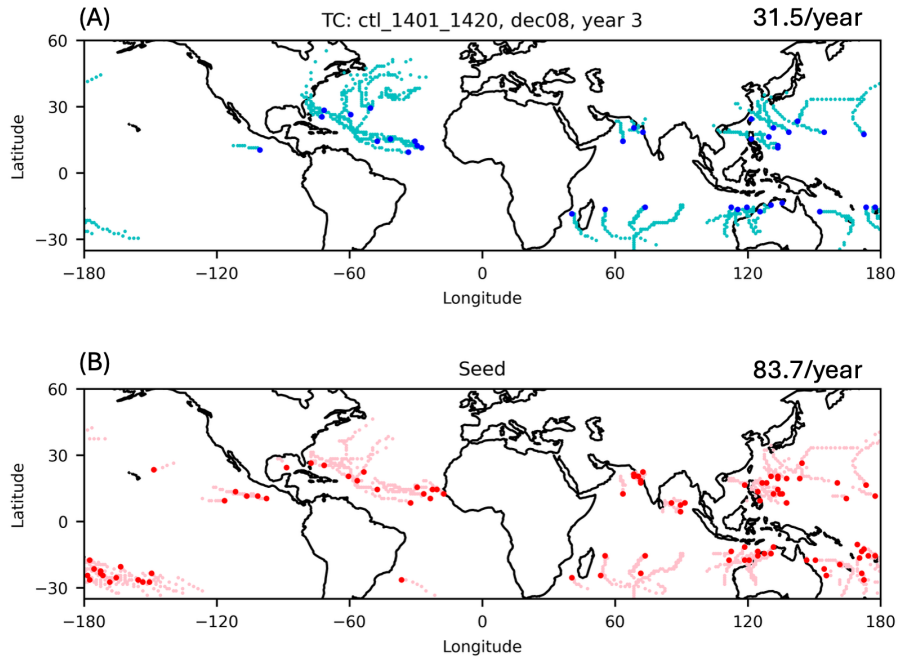


Fig. S5.

An example of geographic distribution of tropical cyclones and seed disturbances from the 73rd ensemble members of Experiment 1. (A) Tropical cyclone track (light blue) and genesis (dark blue), and (B) tropical seed disturbance track (pink) and genesis (red). The average TC number and seed number in 80 ensemble members in the control run are shown on top right of each panel.

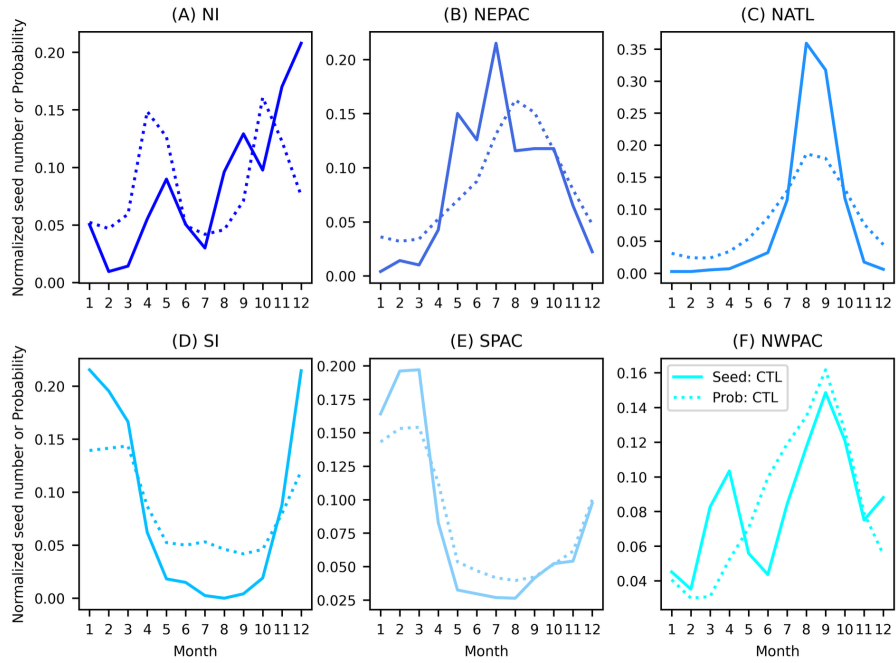


Fig. S6.

The annual cycle of seed disturbance (solid lines) and transition probability (dotted lines) in each basin from the control simulation.

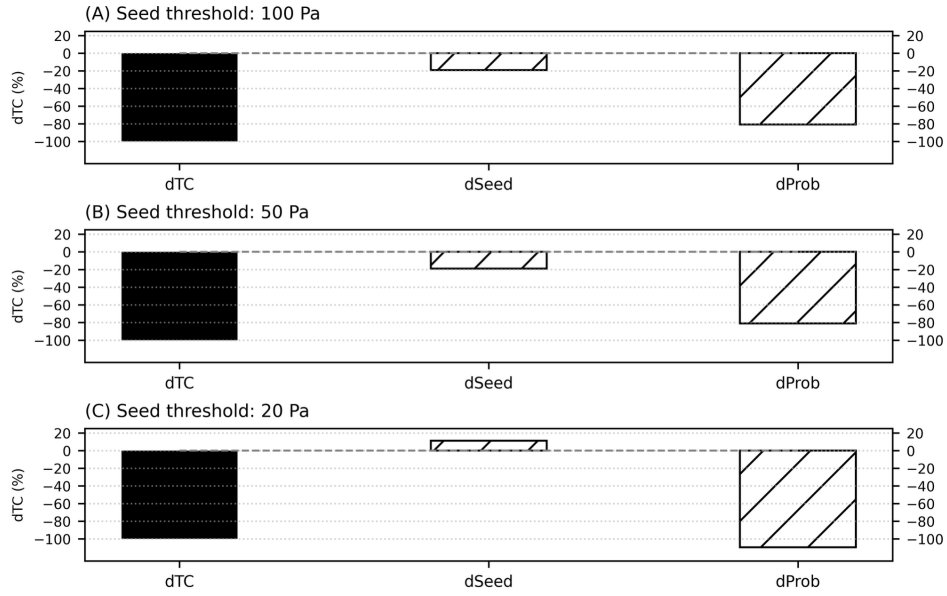


Fig. S7.

Probability change of global TC frequency due to seed or probability. Similar to Fig. 5O, but using different seed definitions: (A) Same as in Fig. 5O, using a sea level pressure threshold of 100 Pa, (B) sea level pressure threshold of 50 Pa, and (C) sea level pressure threshold of 20 Pa.

Seed-to-TC Probability change 1401-1420 to 1461-1480

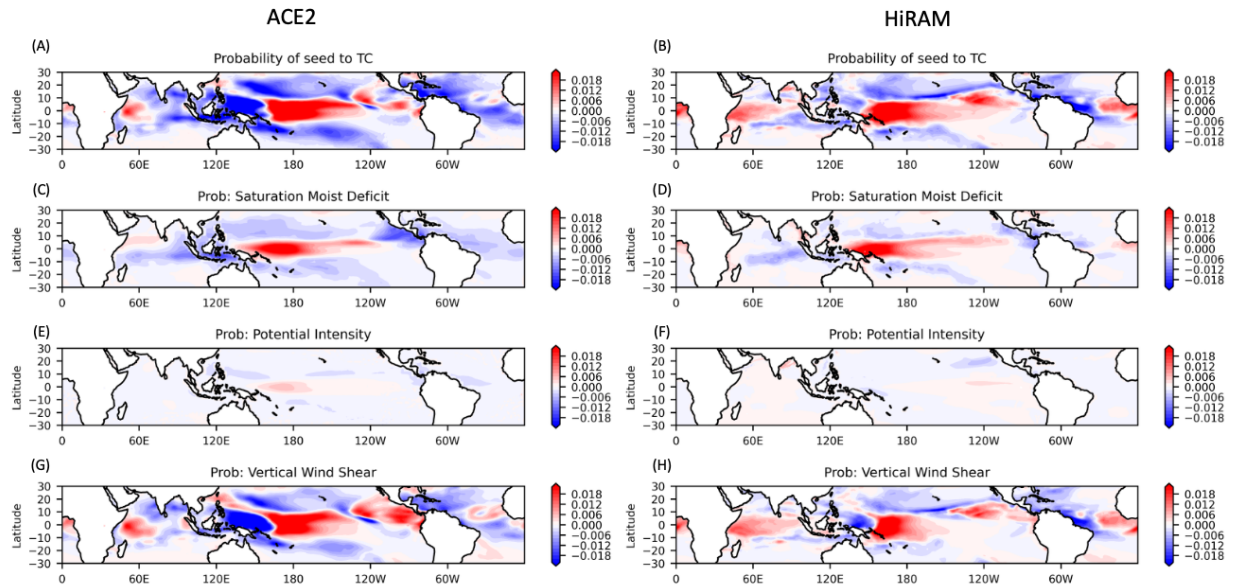


Fig. S8.

Probability change from the control simulation to Experiment 1 based on (A-B) all factors, (C-D) saturation moisture deficit, (E-F) potential intensity, and (G-H) vertical wind shear. The left column (A, C, E, G) presents ACE2-ERA5 results, and the right column (B, D, F, H) presents HiRAM results.

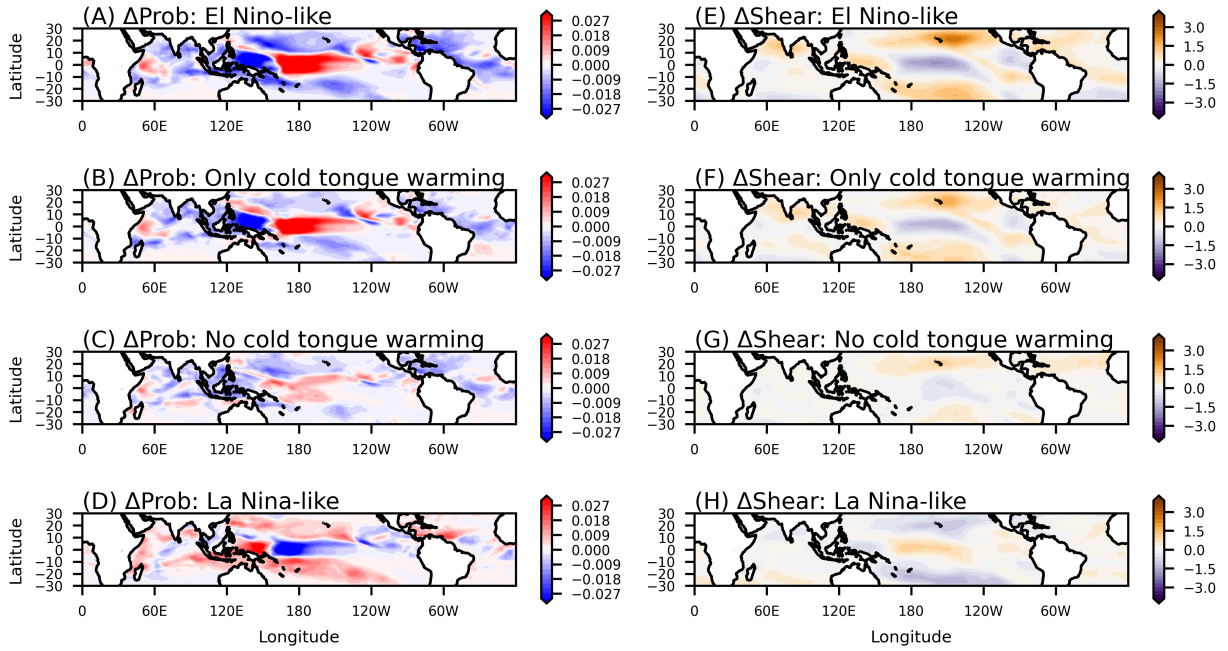


Fig. S9.

(A-D) Change in transition probability in each experiment. (E-H) Change in vertical wind shear in each experiment.

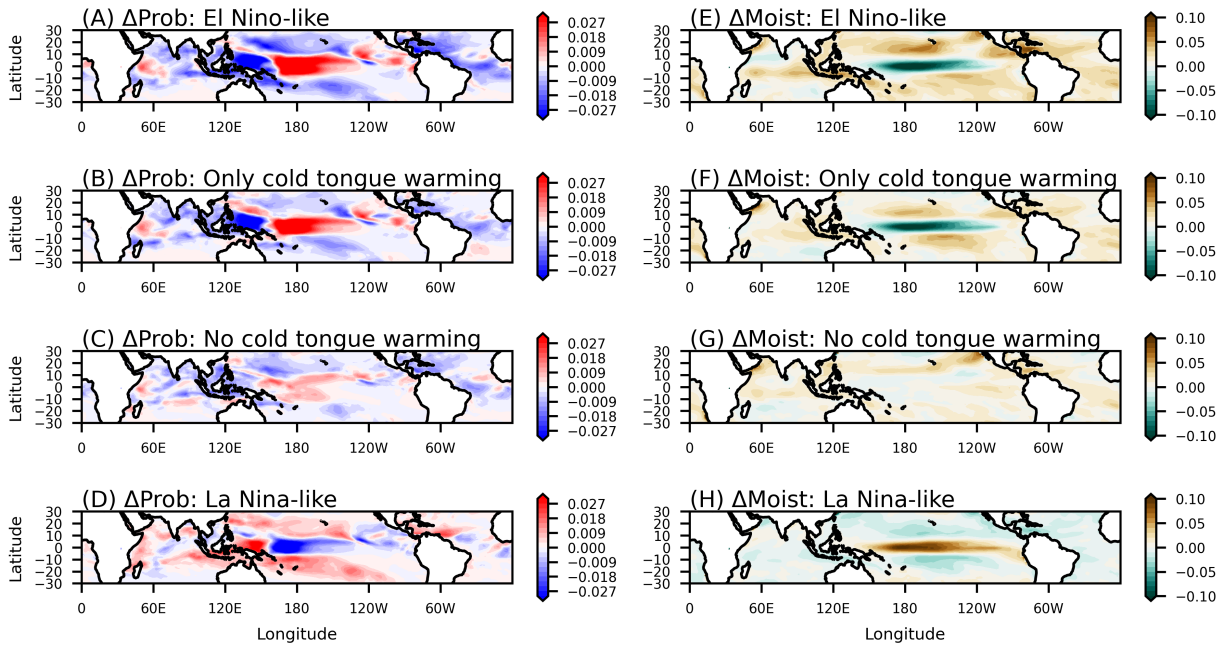


Fig. S10.

(A-D) Change in transition probability in each experiment. (E-H) Change in saturation moisture deficit in each experiment.